Supporting Information

Antonelli et al. 10.1073/pnas.1418907111

SI Materials and Methods

Samples. A total of 61 different troilite nodules from 58 different iron meteorites were analyzed for their sulfur isotopic composition in this study. Examples of the nodules extracted are photographed and shown in Fig. S1. Most of the samples were obtained from the National Museum of Natural History (Smithsonian Institution), using a fine chisel and hammer to chip out small pieces ($\sim$10 mg) of troilite nodules. The samples were picked on a purely visual basis, and variable amounts of graphite (C), cohenite [(Fe,Ni)$_3$C], schreibersite [(Fe,Ni)$_3$P], and silicates, which are relatively common in the troilite nodules, were included in the analyzed samples. Additional troilite was sent from several institutions as noted in Table S1. Sulfur isotope data obtained from the acquired samples is displayed in Table S2.

Sulfur Isotope Measurements. Sulfur is extracted from different mineral phases in a sequential fashion. First, acid volatile sulfur (AVS) is obtained from aliquots of crushed troilite: The samples (5–20 mg) are heated for 3 h in two-necked 50-mL boiling flasks with 20 mL of nitrogen-flushed 5 N HCl through which nitrogen is continuously bubbled; the released H$_2$S$_{(g)}$ (from monosulfides) is carried through a condenser and an acid trap, and is then chemically captured as Ag$_2$S in a slightly acidic trapping solution (containing HNO$_3$ and AgNO$_3$). The apparatus used is the same as described by Forrest and Newman (1).

Chromium-reducible sulfur (CRS) is obtained by changing the capture solution and injecting a reduced Cr (II) solution into the boiling flasks (after 3 h of prior reaction with HCl) after the method of Canfield et al. (2). The CRS solution is allowed to react with the acid residues for an additional 3 h. The small amount of product H$_2$S from chromium reduction of the troilite samples comes from acid-resistant phases within the troilite, possibly from the mineral daubreelite in reduced iron groups (FeCr$_2$S$_4$), or other complex sulfides in other groups. The results for CRS samples large enough to analyze did not show any significant differences in the Δ^{33}S and Δ^{36}S compositions of acid-soluble and acid-resistant minerals (Table S3). Any terrestrial sulfur, in the form of sulfate, is not extracted by these methods. Some of the troilite samples analyzed at the Institut de Physique du Globe de Paris (IPGP) were combined AVS+CRS extractions, achieved by combining the sequential methods used at the University of Maryland (UMD) (Table S4). The precipitated Ag$_2$S is aged in the dark for 1 wk (to remove impurities in the crystals) then centrifuged and rinsed with ultrapure water three times, after which it is allowed to sit overnight in 1 M NH$_4$OH solution to remove impurities, and then again rinsed three times before drying overnight in an oven (at 50 °C).

The fluorination line used in the production of SF$_6$ from Ag$_2$S is dedicated exclusively to meteorite analyses to avoid any possible contaminations from more highly fractionated terrestrial samples. Aliquots of $\sim$3 mg of Ag$_2$S are wrapped in clean aluminum foil and reacted with $\sim$10 times stoichiometric excess of pure F$_2$ in nickel fluorination bombs (at 250 °C overnight), producing SF$_6$ gas and other fluorinated by-products. The excess fluorine is separated cryogenically, as it does not freeze at liquid N$_2$ temperatures ($-$196 °C) whereas both HF and SF$_6$ are trapped at this temperature. After all noncondensable gases are pumped away, the sample is thawed in a small volume and subsequently refrozen using a N$_2$-ethanol slurry (at $-$115 °C), cryogenically trapping HF thereby separating it from the SF$_6$. The SF$_6$ is then purified using gas chromatography on a 12' molecular sieve 5 Å/Hasep Q column with a thermal conduc-

tivity detector, and introduced cryogenically into the cold-finger of a ThermoFinnigan MAT 253 dual-inlet mass spectrometer.

SF$_6$ molecules from the sample and standard gas are ionized to SF$_5^+$ ions in the source of the mass spectrometer (electron impact), focused through lenses, and accelerated down the flight tube through a uniform magnetic field, separating the isotopologues by mass. The ion beams are collected in separate Faraday cups at the detector end of the mass spectrometer that are positioned to measure mass/charge ratios of 127, 128, 129, and 131 (^{32}SF$_5^+$, ^{33}SF$_5^+$, ^{34}SF$_5^+$, and ^{36}SF$_5^+$ respectively). The number of ions hitting each detector can be calculated (ions per second) for each isotopologue by measuring the voltage drops across resistors of known conductance.

Sulfur isotope measurements on the three obtained lunar basalt samples (Table S2) were conducted similarly to those for troilite, but with a slightly different preparation procedure. After cleansing all of the crushing materials in an ultrasonic cleaner (VWR) and methanol bath, lunar basalt samples were crushed using a steel impact mortar and pestle, and further pulverized with an agate mortar and pestle using a small amount ($\sim$5 mL) of ethanol to wet the samples and reduce dust. The resulting slurry was then transferred to the reaction vessels, rinsing with ethanol to ensure quantitative transfer. To minimize oxidation and loss of sulfide, the pulverized samples were immediately placed into the reaction apparatus, where the ethanol was allowed to evaporate under N$_2$. The samples were then reacted with HCl, and then with reduced chromium solution, as described in the methods above.

Quantification of Uncertainty. As the abundance of ^{36}S is the lowest of all stable sulfur isotopes (0.02% of natural abundance, versus 0.79% and 4.29% for ^{33}S and ^{34}S, respectively), its measurement is most susceptible to contamination from traces of other substances. A common source of isobaric interference on m/z position 131 includes contamination from C$_3$F$_5^+$. An attempt at monitoring this contamination is made through the repetitive analysis of International Atomic Energy Agency (IAEA) S1 standard material between meteorite samples (an aliquot of which was fluorinated and processed with every batch of approximately five samples, to also monitor the performance of the GC and fluorination line). In some cases, small $m/z = 131$ contaminations were observed in both the sample and a simultaneously analyzed standard. As a result, samples with obvious contaminations were renormalized back to our long-term accepted values of IAEA S1 (based on their bracketing standard analyses). Measurements of ^{36}SF$_5^+$ also succumb to greater amounts of instrumental noise because the resistor at $m/z = 131$ has the lowest conductivity, which is necessary to obtain a sufficient signal from an isotope of such low abundance. The current of the most abundant ion beam (^{32}SF$_5^+$) was approximately $\sim$10 nA ($\sim$6 billion ions per second) for the average sample size in this study.

For the dominant portion of iron meteorite measurements, the regular amounts of analyses performed per sample at UMD were tripled to decrease the uncertainty of our measurements. Each value reported is the average of 36 individual cycles; in each cycle, the isotopic difference is measured between a sample and our reference gas, which has a known isotopic composition relative to CDT. All results are finally converted to a known reference frame by renormalizing to bracketing IAEA S1 analyses (if necessary), and subsequently normalizing to our repeat measurements of CDT, which defines δ^{3X}S and Δ^{3X}S values of zero.

However, CDT reference material has been observed to possess δ^{34}S variations of $\pm$0.2‰ in different nodules (3), which

contributes to the lower external reproducibility of our measurements for this parameter. To avoid inconsistency, the analyses made in this study were normalized to the average value for repeated measurements of CDT material from a single sample at UMD (Table S3).

During the chemical extraction of sulfur from a sample, the incomplete reaction of sulfides could introduce a kinetic isotope fractionation effect into the captured Ag_2S. In addition, loss of any product H_2S during the extraction (through oxidation or leakage) would also lead to kinetic isotope fractionation. Due to these factors, a great deal of care is taken leak-checking the reaction apparatuses and purging them with N_2 for >30 min before introducing HCl (that has also been degassed separately with N_2 for the same amount of time). For subsequent CRS extractions, the Cr (II) solution is degassed with N_2 before its injection into the reaction flasks, in an ongoing effort to minimize oxygen in the system.

After the Ag_2S is collected, incomplete rinsing could lead to impurities in the subsequent fluorination and could cause the conversion of Ag_2S to SF_6 to be nonquantitative, which could introduce a mass-dependent isotopic fractionation into the sample. All samples are reacted with ~10× stoichiometric excess of F_2 at 250 °C overnight, to promote a full reaction. Although the bombs are degassed and checked for leaks before fluorine introduction, adsorbed water and oxygen (along with possible small leaks and temperature variations) may inhibit the completely quantitative reaction of Ag_2S to SF_6, in turn causing a mass-dependent isotopic fractionation.

Despite the numerous processes preceding the sulfur isotope analyses, duplicate sulfur extractions of five different samples yielded average differences of only 0.07‰, 0.002‰, and 0.15‰ for $\delta^{34}S$, $\Delta^{33}S$, and $\Delta^{36}S$, respectively (Table S3), while six duplicate analyses of a single troilite nodule from the Canyon Diablo IAB iron meteorite yield 2σ s.d. of 0.16‰, 0.008‰, and 0.09‰, for $\delta^{34}S$, $\Delta^{33}S$, and $\Delta^{36}S$, respectively (Table S3). These repeat measurements serve to indicate that the total extraction, purification, and analysis procedures at UMD are well within the range of our reported long-term reproducibility.

However, due to long-term drift in the machine and isotopic variability reported in CDT (3), along with small differences in the methodology of individual operators, it is best to report the external reproducibility of the measurements in this study based on the laboratory's long-term (2 y) reproducibility on IAEA S1 reference material, which is 0.3‰, 0.008‰, and 0.3‰ (2s.d.) for $\delta^{34}S$, $\Delta^{33}S$, and $\Delta^{36}S$, respectively, taking into account the improved counting statistics resulting from the tripled number of analyses performed on each sample.

Interlaboratory Measurements. Fourteen different troilite samples were reanalyzed for their sulfur isotopic compositions at the IPGP, with results shown in Table S4. As can be seen, the IPGP measurements reproduce the sulfur isotopic values we obtained for several important specimens, most notably for the IIIF specimen Cerro del Inca. The average absolute differences between the two laboratories in $\Delta^{33}S$ and $\Delta^{36}S$ for the 14 iron meteorites are 0.006‰ and 0.136‰, respectively, which are well below our stated uncertainties. The linear regression for data obtained at IPGP also yields the same array as that obtained at UMD, when excluding three outlier points that would otherwise control the regression [$\Delta^{36}S/\Delta^{33}S \sim -7$ (Fig. S3)].

However, comparisons of our $\delta^{34}S$ measurements yield an average absolute difference of 0.34‰, which is not a systematic deviation (Table S4). The origin of this difference is unclear. About half of the 14 samples were extracted and precipitated as Ag_2S at UMD. The Ag_2S precipitate was mechanically homogenized and then split in two for each aliquot to be analyzed separately.

Other samples were sent to IPGP as troilite and extracted there into a combined AVS+CRS Ag_2S product. This procedure extracts sulfur from less reactive mineral phases (in addition to troilite), which may account for some of the variability [our own extractions of CRS at UMD had significant deviations from AVS in $\delta^{34}S$ (Table S3)]. It must also be noted that all chemical processes necessary in the extraction and analysis of sulfur isotopes can potentially lead to mass-dependent fractionations, if any product is lost or if any reactions are incomplete; this may be one of the reasons that there are larger interlaboratory variations in $\delta^{34}S$ than in $\Delta^{33}S$ and $\Delta^{36}S$. Despite this fact, the established external reproducibility of the $\Delta^{33}S$ and $\Delta^{36}S$ measurements in this study lends weight to the differences we describe in our paper.

Potential Variability from Noncanonical Mass Dependence. For equilibrium exchange reactions, the exponent which relates the fractionation factor for ^{33}S to ^{34}S is typically between 0.514 and 0.515 (4), but it has been suggested that some kinetic processes can result in an exponent for sulfur that may be as extreme as 0.507 or 0.518, which were calculated to yield a maximum $\Delta^{33}S$ variation of 0.01‰ (compared with the canonical value of 0.515), given the $\delta^{34}S$ range found in iron meteorites. This process does not provide a large enough signal to account for the observed range of $\Delta^{33}S$ (−0.031 to +0.031‰), and evidence for these extreme noncanonical slopes is not provided by the S isotope data.

Nitrogen Isotopes. Photochemical isotope fractionation has also been invoked as an explanation for the large range in $\delta^{15}N$ (~250‰) found in iron meteorites (5–8). However, the few available data make it difficult to establish whether $\Delta^{33}S$ and $\delta^{15}N$ could be related. This is because single iron meteorites can be highly variable in $\delta^{15}N$ (>70‰ range for Canyon Diablo), which might result from analytical artifacts, terrestrial contamination, and/or degassing (9). Furthermore, very few $\Delta^{33}S$ and $\delta^{15}N$ values have been determined for the same meteorite ($n = 10$), and no coupled data exist for groups IC, IIAB, and IIIF. Comparing the available $\delta^{15}N$ and $\Delta^{33}S$ data does not highlight any trends at present, but such a relation might be rediscussed in subsequent studies as more data are acquired.

Photolysis Model for Early Solar Nebula. To model H_2S photolysis in the solar nebula, we used the evolving solar nebula model of Hersant et al. (10), which is the same model used in Pasek et al. (11). We used the time-dependent midplane temperature and disk surface density, but we assumed an isothermal vertical temperature profile, implicitly adding viscous heating. We used the nominal model values in (10), with initial accretion rate $\dot{M}_0 = 5 \times 10^{-6}$ M_{solar} y^{-1}, turbulent viscosity parameter $\alpha = 0.009$, and initial outer disk radius $R_{D0} = 17$ AU. The initial disk mass is 0.24 M_{solar}, low enough to prevent gravitational instability. The accretion rate evolves as

$$\dot{M}(t) = \dot{M}_0 \left(1 + \frac{t}{t_0}\right)^{-s}, \qquad \textbf{[S1]}$$

where $t_o = R_{Do}^2/3\nu_{Do} \sim 3 \times 10^4$ y (11), $s = 1.5$, and ν_{Do} is the turbulent viscosity at the initial disk edge. As the accretion rate decreases with time, the disk surface density and midplane temperature also decrease. We present estimates of the H_2S photolysis rates for two end-member scenarios (high-mass disk vs. low-mass disk) for both solar and subsolar oxygen abundances (C/O = 1.5), to illustrate how much Ly-α photolysis is expected at different periods in solar system history.

We evaluated the H_2S photolysis and mixing timescales assuming a vertically isothermal solar nebula. Our disk has number density given by

$$\rho(R,Z) = \frac{\Sigma(R)}{\sqrt{2\pi}H}\exp\left(-\frac{Z^2}{2H^2}\right), \qquad \textbf{[S2]}$$

where $\Sigma(R)$ is the surface density in g/cm^2, and $\rho(R,Z)$ is the mass density of the nebular gas in g/cm^3 at heliocentric distance R and height above the midplane Z. R_{AU} is defined as $(R/1\ AU)$ and so is dimensionless. The scale height is $H(R) = C_s/\Omega$, where $C_s = (kT/\mu m_H)^{0.5}$ is the sound speed, and the Keplerian orbital frequency is $\Omega = (GM_{sun}/R^3)^{0.5}$, where G is the gravitational constant, M_{sun} is the solar mass, $\mu = 2.37$ is the mean molecular weight of nebular gas, m_H is the proton mass, and k is the Boltzmann constant. It is useful to have the number density of hydrogen nuclei (most of which are in H$_2$) for optical depth calculations. A mean molecular weight of 2.37 corresponds to a H$_2$ fraction of $f_{H2} = 0.82$ and $f_{He} = 0.18$. Considering the most abundant gases only, the gas density is $\rho = m_{H2}\,n_{H2} + m_{He}\,n_{He}$ and the number density of H nuclei is

$$n_H(R,Z) = \frac{2\rho(R,Z)}{m_{H_2} + \dfrac{f_{He}}{1-f_{He}}m_{He}}. \qquad \textbf{[S3]}$$

The photolysis rate coefficient J (molecules per second) for H$_2$S due to Ly-α photons as a function of height from the disk midplane is given by

$$J_{H_2S}(Z) = \int_{Ly\alpha} \sigma_{H2S}\varphi I_{H\ layer}e^{-\tau(z)}d\lambda, \qquad \textbf{[S4]}$$

where $\sigma_{H2S} = 2.8 \times 10^{-17}$ cm^2 is the absorption cross sections for H$_2$S at Ly-α (12), φ is the dissociation probability for H$_2$S (we assume this is unity), and $I_{H\ layer}$ is the Ly-α intensity at the base of the H atom layer high in the disk. The H atom layer isotropically scatters Ly-α photons such that the base of the H atom layer blankets the interior disk in Ly-α. To first order, $I_{H\ layer}$ is $\sim 1/2$ the Ly-α intensity incident on the H layer at $R = 1$ AU, but now directed downward toward the disk midplane (13). At Ly-α, the main absorbers are H$_2$O, dust and H$_2$S, so the Ly-α optical depth τ is given by

$$\tau(Z) = \sigma_{H_2S}N_{H_2S}(Z) + \sigma_{H_2O}N_{H_2O}(Z) + \sigma_{dust}N_{dust}(Z), \qquad \textbf{[S5]}$$

where $N_x(Z)$ is the column number density of absorber x above height Z to the H atom layer. We compute the column density as

$$N_x(Z) \approx \int_Z^\infty n_x(0)e^{-\frac{z^2}{2H^2}}dz, \qquad \textbf{[S6]}$$

where H is the disk scale height, given in Table 1, and where we approximate the height of the H atom layer to be at infinity (at $R = 1$ AU, the H atom layer extends vertically from $Z \sim 0.6$–1.0 AU in the model of ref. 13). In our isothermal model, such heights correspond to implausibly low gas densities. Accounting for upper disk heating due to EUV radiation yields an increasing gas temperature in the upper regions of the disk, so the scale height and gas densities are larger than an isothermal model would predict. Here, for simplicity, we assume gas column density above the H atom layer is negligible. Using a two-term expansion for the complementary error function on Eq. **S6**, the column density is

$$N_x(Z) \approx n_x(Z)\frac{H^2}{Z}\left(1-\frac{H}{Z}\right) \qquad \textbf{[S7]}$$

To determine the depth of penetration of Ly-α into the disk from the overlying H atom layer, we computed the optical depths for H$_2$O, H$_2$S, and dust, shown summed in Eq. **S5**. The fractions of CO, H$_2$O, and H$_2$S relative to H are $\sim 2.7 \times 10^{-4}$, 1.2×10^{-4}, and 1.3×10^{-5}, respectively, assuming solar elemental abundances (14), and a fraction of O atoms trapped in SiO$_3$ bonds (pyroxene dust). The dust optical depth is expressed relative to the column density of H atoms as $\tau_{dust} = \gamma\sigma_{dust}N_H(Z)$ where $\sigma_{dust} = 5.6 \times 10^{-22}$ cm^2 and $\gamma \sim 0.6$ for 1-μm dust. Table S6 shows the Ly-α optical depths for all three absorbers considered here for a high-mass disk and low-mass disk [<50 Ky and <500 Ky, respectively (two snapshots in protoplanetary disk evolution)] corresponding to the Hersant et al. disk model (10). From Table S6, H$_2$O is the dominant Ly-α absorber for the case with solar H$_2$O abundance in both disks, and limits H$_2$S photolysis to between $Z = 0.3$–0.25 AU, and between $Z = 0.25$–0.2 AU, respectively, assuming photolysis will stop at optical depths higher than an order of about 1. For the case with reduced water abundance (corresponding to C/O = 1.5 in ref. 12), H$_2$O, H$_2$S, and dust are comparable (within a factor of 2) in Ly-α absorption, implying that H$_2$S photolysis will occur slightly deeper in the disk.

Photolysis in the nebula will occur as long as turbulently mixed gas is available in the photoactive zone. A more refined calculation for penetration depth takes into account the photolysis timescale for an H$_2$S molecule at different heights in the disk and at 1 AU, and yields the depth at which this does not exceed the timescale for turbulent mixing (Table 1), which is in agreement with our coarser estimates. For example, in the high-mass (<50 Ky) disk with solar C/O ratio, $J_{H2S}(Z) = 4.2 \times 10^{-4}\exp[-\tau(Z)]$ s^{-1}, where $\tau(Z) = 2.2 \times 10^6(H/Z)(1 - H/Z)\exp(-Z^2/2H^2)$ and $t_\nu^{-1}(Z) = 7.3 \times 10^{-12}(1\ AU/Z)^2$ s^{-1}. Solving graphically yields a penetration depth (Z_{ph}) of 0.29 AU for this case (Table 1).

As discussed in the text, H$_2$S photolysis experiments at Ly-α (15) give a maximum Δ^{33}S of approximately (negative) 1.5‰ in elemental sulfur, suggesting that $\sim 2\%$ of total disk H$_2$S needs to be photolyzed in the region of the nebula where troilite grains were produced. Because this is a much larger fraction of H$_2$S than represented in the photoactive zone at any one time, vertical mixing of the nebular gas is needed to dredge up enough H$_2$S to the Ly-α photolysis zone. Assuming that turbulent vertical mixing was present due to a magnetorotational instability (MRI) at 1 AU (at 700 K, there may still have been enough Na$^+$ and/or K$^+$ present to allow coupling to the magnetic field, although higher temperatures are more favorable), we estimate the vertical mixing time to height Z as $t_\nu \sim Z^2/\alpha_\nu c_s H$, where α_ν is the turbulent viscosity parameter. For fairly strong MRI-induced turbulence, the viscosity parameter is typically $\alpha_\nu \sim 0.01$ [in the Hersant et al. (10) model, $\alpha_\nu = 0.009$, which we assumed here]. The mixing time (t_ν) for the solar and subsolar O cases is ~ 200–300 y (Table 1). The timescales for the number of overturns required to produce the observed Δ^{33}S signatures in a high-mass and low-mass disk, at both solar and subsolar oxygen abundances, are tabulated in Table 1, and range from ~ 200 Ky to ~ 10 Ky, which is consistent with a preaccretionary origin for the anomalous sulfur signals.

A final consideration to be taken into account relates to the inference about the starting composition of sulfur in the inner solar system. It is possible that the sulfur isotopic composition of the Sun is different from the inferred composition that we take as a starting point for interpreting the sulfur isotopic variability of meteoritic, lunar, and planetary materials. It is known from secondary ion mass spectrometry measurements (e.g., ref. 16) that nucleosynthetic heterogeneities exist in presolar materials. If the composition of sulfur that made up the magmatic iron meteorites started with a ^{33}S enrichment relative to the Earth, Moon, Mars, chondrites and nonmagmatic iron meteorites, a nucleosynthetic origin could be possible and an implication could be that these other inner solar system bodies also acquired

a nucleosynthetic sulfur component. We consider the present dataset, however, to be more simply explained by a singular reservoir that was fractionated into the magmatic iron and achondrite groups. The strong prevalence of chondritic $\Delta^{33}S$ signatures [means and uncertainties (2SE): carbonaceous chondrites $+0.012 \pm 0.014\permil$; ordinary chondrites $+0.005 \pm 0.014\permil$; enstatite chondrites $-0.007 \pm 0.010\permil$ (17, 18)] found in solar system materials such as the IAB iron meteorites [$+0.004 \pm 0.002\permil$ (2SE)] and the least-altered samples of larger planetary bodies like the Earth, Moon, and Mars (19–22), along with our data for negative $\Delta^{33}S$ in solar system materials, supports the suggestion that bulk solar system $\Delta^{33}S$ was chondritic, and that deviations from this value are most likely the results of inner solar system photochemistry.

1. Forrest J, Newman L (1977) Silver-110 microgram sulfate analysis for the short time resolution of ambient levels of sulfur aerosol. *Anal Chem* 49(11):1579–1584.
2. Canfield DE, Raiswell R, Westrich JT, Reaves CM, Berner RA (1986) The use of chromium reduction in the analysis of reduced inorganic sulfur in sediments and shales. *Chem Geol* 54(1-2):149–155.
3. Beaudoin G, Taylor BE, Rumble D-III, Thiemens MH (1994) Variations in the sulfur isotope composition of troilite from the Cañon Diablo iron meteorite. *Geochim Cosmochim Acta* 58(19):4253–4255.
4. Farquhar J, Johnston DT, Wing BA (2007) Implications of conservation of mass effects on mass-dependent isotope fractionations: Influence of network structure on sulfur isotope phase space of dissimilatory sulfate reduction. *Geochim Cosmochim Acta* 71(24):5862–5875.
5. Franchi IA, Wright IP, Pillinger CT (1993) Constraints on the formation conditions of iron-meteorites based on concentrations and isotopic compositions of nitrogen. *Geochim Cosmochim Acta* 57(13):3105–3121.
6. Mathew KJ, Palma RL, Marti K, Lavielle B (2000) Isotopic signatures and origin of nitrogen in IIE and IVA iron meteorites. *Geochim Cosmochim Acta* 64(3):545–557.
7. Prombo CA, Clayton RN (1993) Nitrogen isotopic compositions of iron meteorites. *Geochim Cosmochim Acta* 57(15):3749–3761.
8. Chakraborty S, et al. (2014) Massive isotopic effect in vacuum UV photodissociation of N_2 and implications for meteorite data. *Proc Natl Acad Sci USA* 111(41):14704–14709.
9. Yokochi R, Marty B (2006) Fast chemical and isotopic exchange of nitrogen during reaction with hot molybdenum. *Geochem Geophys Geosyst* 7:Q07004.
10. Hersant F, Gautier D, Hure J-M (2001) A two-dimensional turbulent model for the solar nebula constrained by D/H measurements in the solar system: Implications for the formation of giant planets. *Astrophys J* 554:391–407.
11. Pasek MA, et al. (2005) Sulfur chemistry with time-varying oxygen abundance during solar system formation. *Icarus* 175(1):1–14.
12. Brownsword RA, Laurent T, Vatsa RA, Volpp H-R, Wolfrum J (1996) Photodissociation dynamics of HNCO at 248 nm. *Chem Phys Lett* 258(1-2):164–170.
13. Bethell TJ, Bergin EA (2011) The propagation of Ly-α in evolving protoplanetary disks. *Astrophys J* 739(2):78.
14. Asplund M, Grevesse N, Sauval AJ, Scott P (2009) The chemical composition of the sun. *Annu Rev Astron Astrophys* 47:481–522.
15. Chakraborty S, Jackson TL, Ahmed M, Thiemens MH (2013) Sulfur isotopic fractionation in vacuum UV photodissociation of hydrogen sulfide and its potential relevance to meteorite analysis. *Proc Natl Acad Sci USA* 110(44):17650–17655.
16. Fujiya W, Hoppe P, Zinner E, Pignatari M, Herwig F (2013) Evidence for radiogenic sulfur-32 in type AB presolar silicon carbide grains? *Astrophys J* 776:L29.
17. Gao X, Thiemens MH (1993) Isotopic composition and concentration of sulfur in carbonaceous chondrites. *Geochim Cosmochim Acta* 57(13):3159–3169.
18. Gao X, Thiemens MH (1993) Variations of the isotopic composition of sulfur in enstatite and ordinary chondrites. *Geochim Cosmochim Acta* 57(13):3171–3176.
19. Labidi J, Cartigny P, Moreira M (2013) Non-chondritic sulphur isotope composition of the terrestrial mantle. *Nature* 501(7466):208–211.
20. Peters M, et al. (2010) Sulfur cycling at the Mid-Atlantic Ridge: A multiple sulfur isotope approach. *Chem Geol* 269(3-4):180–196.
21. Wing BA, Farquhar J (2014) Planetary sulfur isotopic baseline from lunar basalts. *Geochim Cosmochim Acta*, in press.
22. Franz HB, et al. (2014) Isotopic links between atmospheric chemistry and the deep sulphur cycle on Mars. *Nature* 508(7496):364–368.
23. McEwing CE, Thode HG, Rees CE (1980) Sulphur isotope effects in the dissociation and evaporation of troilite: A possible mechanism for ^{34}S enrichment in lunar soils. *Geochim Cosmochim Acta* 44:565–571.
24. Rai VK, Thiemens MH (2007) Mass-independently fractionated sulfur components in chondrites. *Geochim Cosmochim Acta* 71(5):1341–1354.
25. Farquhar J, Jackson TL, Thiemens MH (2000) A ^{33}S enrichment in ureilite meteorites: Evidence for a nebular sulfur component. *Geochim Cosmochim Acta* 64(10):1819–1825.
26. Ludwig KR (2001) *Isoplot 3.0—A Geochronological Toolkit for Microsoft Excel.* Special Publication 4 (Berkeley Geochronol Cent, Berkeley, CA).
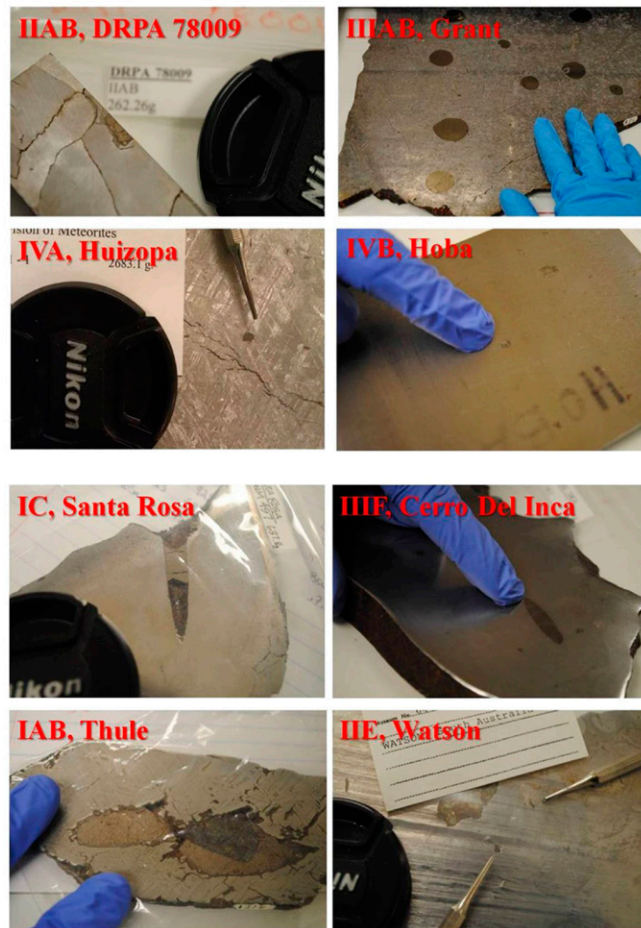
Fig. S1. Photos of troilite nodules from one of each iron meteorite group analyzed. As shown above, the troilite nodules vary in size from several centimeters to few millimeters, with variable degrees of impurity, containing possible inclusions of graphite, cohenite [$(Fe,Ni)_3C$], silicates, and/or schreibersite [$(Fe,Ni)_3P$].
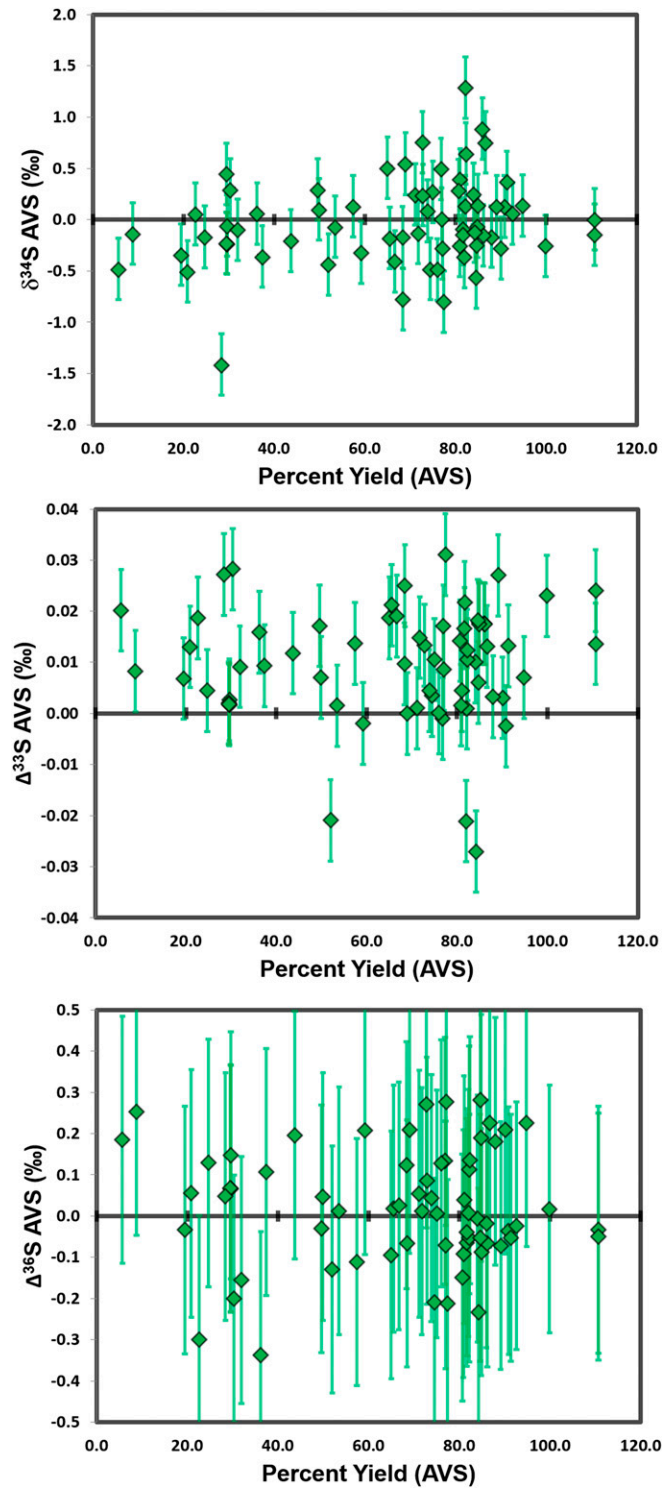
Fig. S2. Obtained $\delta^{34}S$, $\Delta^{33}S$, and $\Delta^{36}S$ data versus percent ideal yields (pure troilite) of AVS extractions. Error bars represent 2s.d. long-term uncertainties on $\delta^{34}S$, $\Delta^{33}S$, and $\Delta^{36}S$ of 0.3‰, 0.008‰, and 0.3‰, respectively. Impurities in the troilite nodule have not been shown to affect sulfur extraction efficiencies; there is no correlation between the sulfur isotopic composition of troilite and its abundance in an analyzed sample.
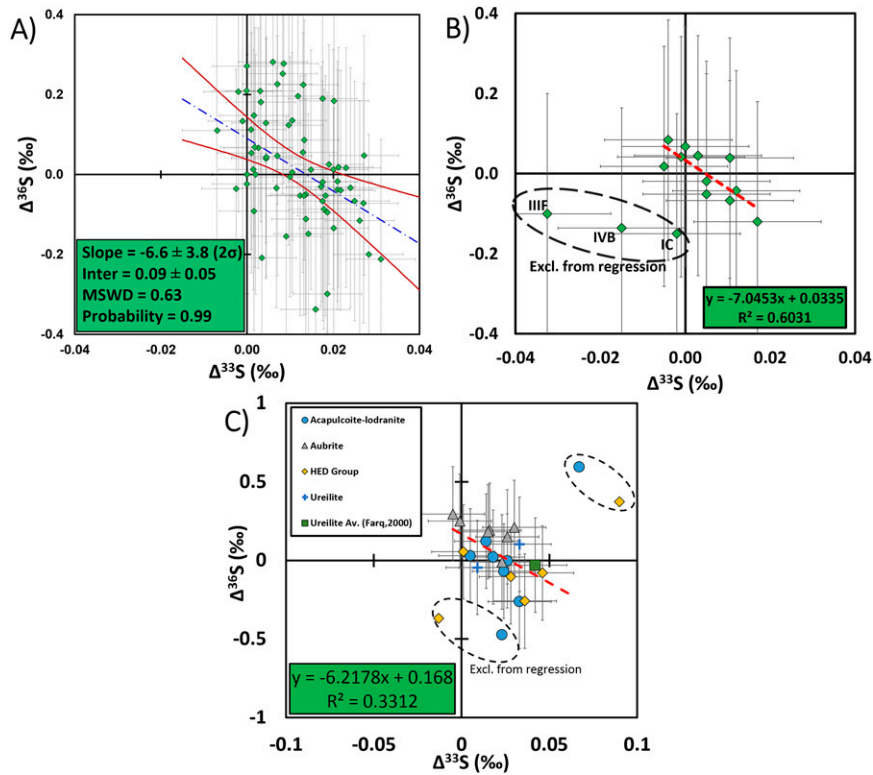
Fig. S3. Linear regressions of (*A*) Iron meteorite analyses at UMD, (*B*) duplicate analyses at IPGP, and (*C*) available sulfur isotopic data for bulk achondrites, in $\Delta^{36}S$ vs. $\Delta^{33}S$ space. (*A*) Regression and error envelope for iron meteorites from groups with more than eight analyzed members, defines $\Delta^{36}S/\Delta^{33}S$ array of -7 ± 4 (2s.d.). (*B*) Linear regression of iron meteorite analyses from IPGP, excluding three outliers, defines a weak $\Delta^{36}S/\Delta^{33}S$ array of -7. (*C*) Linear regression of available data for bulk achondrites (24, 25), defines $\Delta^{36}S/\Delta^{33}S$ array of -6 ± 6 (2s.d.) (excluding four outliers in $\Delta^{36}S$). These arrays are consistent with each other and, given uncertainties and small spread of data, with Lyman-α photolysis experiments on H_2S (13) ($\Delta^{36}S/\Delta^{33}S$ of -3). Slope errors calculated using ref. 26.
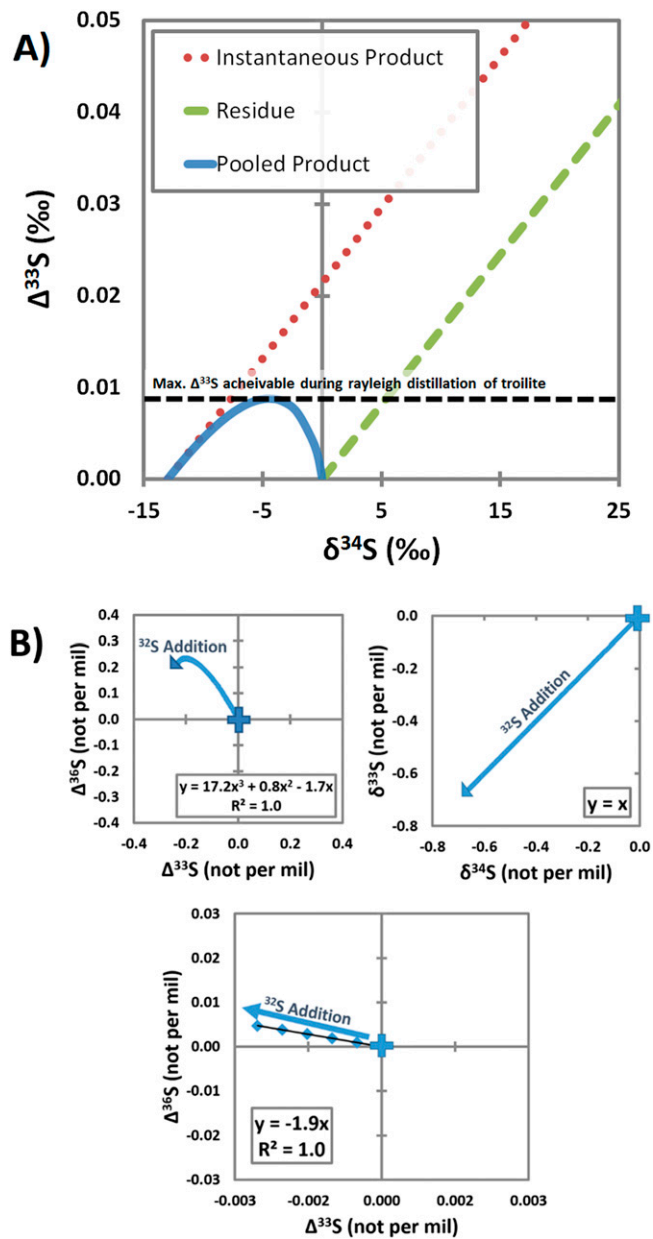
Fig. S4. (*A*) $\Delta^{33}S$ variations from mixing of products and reactants during Rayleigh distillation of troilite. (*B*) Modeled nucleosynthetic injection of a pure ^{32}S component on the sulfur isotopic composition of CDT. (*A*) Modeled variations in $\Delta^{33}S$ due to Rayleigh distillation during evaporation of troilite, using data from ref. 23, produces a max possible $\Delta^{33}S$ of 0.009‰. (*B*) Modeled injection of ^{32}S, as found in certain presolar SiC grains (16), leads to a unidirectional departure from CDT with a $\Delta^{36}S/\Delta^{33}S$ array of −1.9 (about the origin).

Table S1. List of iron meteorites analyzed in this study

Name	Group	Source	Name	Group	Source
Osseo	IAB-comp	USNM925	Patos de Minas (Hex)	IIAB	USNM6844
ALHA77290	IAB-MG	USNM6361	Watson	IIE	USNM6483
Bogou	IAB-MG	USNM2245	Acuna	IIIAB	NHM
Burkett	IAB-MG	USNM586	Apoala	IIIAB	ME1009-1A
Campo del Cielo	IAB-MG	USNM5615	Apoala 2	IIIAB	ME1009-3B
Canyon Diablo	IAB-MG	ME2108-1	Loreto	IIIAB	USNM1507
Deelfontain	IAB-MG	USNM3275	Wabar	IIIAB	USNM1564
Hope	IAB-MG	USNM3476	Waingaromia	IIIAB	USNM5771
Idaho	IAB-MG	USNM1652	Cape York	IIIAB	USNM5726
Wichita County	IAB-MG	ME885-1	Grant	IIIAB	USNM836
Mundrabilla 2	IAB-Mund	WAM13583	Thule	IIIAB	USNM4856
Mundrabilla	IAB-Mund	USNM5914	Kenton County	IIIAB	USNM2848
Waterville	IAB-Mund	USNM1512	Costilla Peak	IIIAB	ME856-1
Pitts	IAB-Pitts	USNM1378	La Porte	IIIAB	ME2269-2
Woodbine	IAB-Pitts	USNM2169	Sacramanto Mtns	IIIAB	AMNH4209
Bischtube	IAB-sLL	USNM229	Casas Grandes	IIIAB	USNM369A2
Goose Lake	IAB-sLL	USNM1332	Trenton	IIIAB	USNM2173
Toluca	IAB-sLL	USNM1214	MET0040	IIIAB	USNM7080-2
Lamesa, Texas	IAB-sLM	USNM6250	Cerro del inca	IIIF	USNM7062
Malta Hohe	IAB-sLM	USNM6482	Moonbi	IIIF	USNM4853
Mertzon	IAB-ung	USNM1435	Altonah	IVA	USNM863
Mesa Verde Park	IAB-Ung	USNM645	Bushman Land	IVA	USNM2515A22
Santa Rosa	IC	USNM457	Duchesne	IVA	USNM2181
Santa Rosa 2	IC	ME762-1	Gibeon	IVA	AMNH775
DRPA 78008/10	IIAB	UCSD	Harriman	IVA	USNM6072
DRPA 78009	IIAB	USNM6363	Huizopa	IVA	USNM871-1
Indian Valley	IIAB	USNM323	Maria Elena	IVA	USNM1221-32
Keen Mountain	IIAB	USNM1513	Mart	IVA	USNM221
Mayodan	IIAB	USNM1487	S.J. Nepomuceno	IVA	USNM6881
North Chile	IIAB	USNM2306	Hoba	IVB	USNM6506
Old Woman	IIAB	USNM6359-17			

USNM, National Museum of Natural History (Smithsonian Institution); ME, Field Museum, Chicago; WAM, Museum of Western Australia; UCSD, University of California San Diego (Mark Thiemens); AMNH, American Museum of Natural History; NHM, Naturhistoriches Museum, Austria.

Table S2. Sulfur isotopic analyses of iron meteorite troilite and three lunar basalts

Name	Class	δ^{34}S, ‰	Δ^{33}S, ‰	Δ^{36}S, ‰	Name	Class	δ^{34}S, ‰	Δ^{33}S, ‰	Δ^{36}S, ‰
Osseo	IAB-comp	0.393	0.004	0.040	Acuna	IIIAB	0.004	0.024	−0.033
ALHA77290	IAB-MG	0.496	−0.001	0.134	Acuna (Fluo 2)	IIIAB	−0.146	0.014	−0.050
Bogou	IAB-MG	0.252	0.010	−0.006	Apoala	IIIAB	0.056	0.019	−0.299
Burkett	IAB-MG	0.132	0.001	0.112	Apoala 2	IIIAB	−.179	0.021	0.018
Campo del Cielo	IAB-MG	−0.168	0.004	0.129	Loreto	IIIAB	0.272	0.011	0.005
Campo del Cielo (AVS2)	IAB-MG	−0.137	0.008	0.253	Wabar	IIIAB	−0.205	0.012	0.196
Canyon Diablo	IAB-MG	−0.277	0.003	0.209	Waingaromia	IIIAB	1.289	0.012	−0.053
Deelfontain	IAB-MG	−0.232	0.003	0.066	Cape York	IIIAB	0.367	0.013	−0.053
Deelfontein (Fluo2)	IAB-MG	−0.058	0.002	0.148	Grant	IIIAB	0.239	0.013	0.086
Hope	IAB-MG	−0.254	0.002	−0.092	Thule	IIIAB	0.287	0.014	−0.149
Idaho	IAB-MG	−0.069	0.001	0.012	Kenton County	IIIAB	−0.130	0.015	0.012
Wichita County	IAB-MG	−0.480	0.003	−0.209	Costilla Peak	IIIAB	−0.562	0.018	−0.053
Mundrabilla 2	IAB-Mund	0.128	−0.003	−0.036	La Porte	IIIAB	0.505	0.019	−0.095
Mundrabilla	IAB-Mund	−0.127	−0.007	0.110	Sacramanto Mtns	IIIAB	0.025	0.020	0.013
Waterville	IAB-Mund	−0.228	0.002	0.068	Grant	IIIAB	0.100	0.021	−0.038
Pitts	IAB-Pitts	−0.319	−0.002	0.207	Casas Grandes	IIIAB	−0.141	0.022	−0.040
Woodbine	IAB-Pitts	0.099	0.007	0.047	Trenton	IIIAB	0.128	0.027	−0.072
Woodbine (Fluo2)	IAB-Pitts	0.086	0.004	0.044	MET0040	IIIAB	0.294	0.028	−0.200
Bischtube	IAB-sLL	0.245	0.001	0.054	**IIIAB Average**		**0.122**	**0.018**	**−0.045**
Goose Lake	IAB-sLL	−0.167	0.003	0.181					
Goose Lake (AVS2)	IAB-sLL	−0.247	0.006	0.282	Cerro del inca	IIIF	−0.117	−0.027	−0.233
Toluca	IAB-sLL	0.546	0.000	0.209	Cerro del Inca-re	IIIF	0.253	−0.029	−0.136
Lamesa, Texas	IAB-sLM	0.752	0.013	0.225	Cerro del inca-re2	IIIF	0.207	−0.031	−0.110
Malta Hohe	IAB-sLM	0.644	0.011	0.135	Cerro del Inca*	IIIF	0.463	−0.033	−0.100
Mertzon	IAB-ung	−0.171	0.010	0.124	Moonbi	IIIF	−0.365	−0.021	0.007
Mertzon (AVS2)	IAB-ung	−0.277	0.009	0.277	Moonbi (AVS2)	IIIF	−0.435	−0.021	−0.130
Mesa Verde Park	IAB-ung	0.139	0.007	0.226	St. Genevieve Cnty[†]	IIIF	0.240	−0.024	−0.256
	IAB Average	**0.026**	**0.004**	**0.109**	**IIIF Average**		**0.035**	**−0.027**	**−0.137**
Santa Rosa	IC	0.008	0.017	−0.070	Altonah	IVA	−0.405	0.019	0.025
Santa Rosa 2	IC	−0.087	0.017	−0.064	Bushman Land	IVA	−0.480	0.020	0.185
					Duchesne	IVA	−0.255	0.023	0.017
					Gibeon	IVA	0.097	0.021	−0.017
DRPA 78008/10	IIAB	0.022	0.026	−0.115	Harriman	IVA	−0.799	0.031	−0.212
DRPA 78008/10 (Fluo2)	IIAB	−0.057	0.020	−0.134	Huizopa	IVA	−0.775	0.025	−0.066
DRPA 78009	IIAB	0.888	0.018	−0.019	Maria Elena	IVA	−1.414	0.027	0.047
Indian Valley	IIAB	−0.343	0.007	−0.034	S.J. Nepomuceno	IVA	−0.505	0.013	0.055
Keen Mountain	IIAB	0.131	0.014	−0.112	S.J. Nepomuceno (Fluo2)	IVA	0.294	0.017	−0.031
Mayodan	IIAB	0.059	0.016	−0.337	**IVA Average**		**−0.471**	**0.022**	**0.000**
North Chile	IIAB	0.143	0.018	−0.087					
Old Woman	IIAB	−0.096	0.009	−0.155	Hoba	IVB	−0.485	0.000	0.128
Patos de Minas (Hex)	IIAB	−0.151	0.018	−0.066					
Patos de Minas (Hex) (AVS2)	IIAB	−0.068	0.017	0.190	10057.271	Lunar basalt	0.697	0.001	−0.022
	IIAB Average	**0.053**	**0.016**	**−0.087**	12022.281	Lunar basalt	0.473	−0.009	−0.027
					70017.598.67	Lunar basalt	0.667	−0.004	0.434
Watson	IIE	−0.361	0.009	0.106	**Lunar Average**		**0.612**	**−0.004**	**0.128**
Watson-re	IIE	−0.025	0.011	−0.020	MORB Glasses[‡]	**Mantle Average[‡]**	**−1.1**	**0.005**	**0.05**
					Lunar Basalts[§]	**Lunar Average[§]**	**0.57**	**0.008**	**0.2**

AVS2, duplicate extraction of initial troilite; Fluo2, duplicate fluorination of Ag$_2$S; re, remeasurement of SF$_6$ after long-term storage. Averages are in bold.
*Duplicate analysis of Cerro from IPGP.
[†]St. Genevieve County data from ref. 1.
[‡]Mantle average from ref. 2.
[§]Lunar average from ref. 3. Long-term uncertainties are 0.3‰, 0.008‰, 0.3‰ (2σ) for δ^{34}S, Δ^{33}S, and Δ^{36}S, respectively.

1. Gao X, Thiemens MH (1991) Systematic study of sulfur isotopic composition in iron meteorites and the occurrence of excess ^{33}S and ^{36}S. *Geochim Cosmochim Acta* 55(9):2671–2679.
2. Labidi J, Cartigny P, Moreira M (2013) Non-chondritic sulphur isotope composition of the terrestrial mantle. *Nature* 501(7466):208–211.
3. Wing BA, Farquhar J (2014) Planetary sulfur isotopic baseline from lunar basalts. *Geochim Cosmochim Acta*, in press.

Table S3. Variability in samples and measurements

Name	Group	$\delta^{34}S$, ‰	$\Delta^{33}S$, ‰	$\Delta^{36}S$, ‰	$\delta^{34}S_{(1-2)}$, ‰	$\Delta^{33}S_{(1-2)}$, ‰	$\Delta^{36}S_{(1-2)}$, ‰	SF_6, torr
Chromium-reducible sulfur analyses*								
Goose Lake CRS	IAB-sLL	1.248	0.006	—	1.455	0.001	—	0.282
Mertzon CRS	IAB-Ung	−0.528	0.009	—	−0.304	0	—	0.485
Santa Rosa CRS	IC	0.803	0.014	0.073	0.842	−0.003	0.141	3.454
Acuna CRS	IIIAB	0.129	0.021	−0.007	0.125	−0.003	0.026	1.522
Apoala 2 CRS	IIIAB	−0.511	0.015	−0.03	−0.45	−0.005	0.11	3.228
Average difference (CRS-AVS)					**0.635**	**0.002**	**0.092**	
Std Dev. (1σ)					0.803	0.003	0.059	
Different nodules†								
Mundrabilla	IAB-Mund	−0.127	−0.007	0.11	—	—	—	—
Mundrabilla 2	IAB-Mund	0.128	−0.003	−0.036	−0.255	−0.004	0.146	—
Santa Rosa	IC	0.008	0.017	−0.07	—	—	—	—
Santa Rosa 2	IC	−0.087	0.017	−0.064	0.094	0	−0.006	—
Apoala	IIIAB	0.056	0.019	−0.299	—	—	—	—
Apoala 2	IIIAB	−0.179	0.021	0.018	0.235	−0.003	−0.318	—
Average difference (different nodules)					**0.195**	**0.002**	**0.156**	
Std Dev. (1σ)					0.252	0.002	0.236	
Extraction duplicates at UMD†								
Campo del Cielo	IAB-MG	−0.168	0.004	0.129	—	—	—	—
Campo del Cielo (AVS2)	IAB-MG	−0.137	0.008	0.253	−0.031	−0.004	−0.124	—
Goose Lake	IAB-sLL	−0.167	0.003	0.181	—	—	—	—
Goose Lake (AVS2)	IAB-sLL	−0.247	0.006	0.282	0.08	−0.003	−0.1	—
Mertzon	IAB-ung	−0.171	0.01	0.124	—	—	—	—
Mertzon (AVS2)	IAB-ung	−0.277	0.009	0.277	0.106	0.001	−0.154	—
Moonbi	IIIF	−0.365	−0.021	0.007	—	—	—	—
Moonbi (AVS2)	IIIF	−0.435	−0.021	−0.13	0.07	0	0.137	—
Patos de Minas (Hex)	IIAB	−0.151	0.018	−0.066	—	—	—	—
Patos de Minas (Hex) (AVS2)	IIAB	−0.068	0.017	0.19	−0.084	0	−0.256	—
Average difference between sulfur extractions					**0.074**	**0.002**	**0.154**	
Std Dev. (1σ)					0.082	0.002	0.145	
Measurement reproducibility of CDT								
(incl. sulfur extraction)								
CDT(07)-USNM6275-1/6-A	IAB-MG	0.115	−0.005	−0.076	—	—	—	—
CDT(07)-USNM6275-2/6-A	IAB-MG	−0.074	0.003	0.024	—	—	—	—
CDT(07)-USNM6275-3/6-A	IAB-MG	0.072	0.003	0	—	—	—	—
CDT(07)-USNM6275-4/6-A	IAB-MG	0.014	−0.004	−0.004	—	—	—	—
CDT(07)-USNM6275-5/6-A	IAB-MG	−0.04	0.003	−0.001	—	—	—	—
CDT(07)-USNM6275-6/6-A	IAB-MG	−0.086	0.001	0.057	—	—	—	—
Average		**0**	**0**	**0**	—	—	—	—
Std. Dev (2σ)		0.163	0.008	0.087				

*Samples with SF_6 pressures of less than 1 torr do not yield reliable $\Delta^{36}S$ data; average differences (bold) are from absolute values.
†Average differences (bold) are calculated from absolute values.

Table S4. Interlaboratory sulfur isotope measurement comparisons for 14 samples

Name	Group	δ^{34}S, ‰	Δ^{33}S, ‰	Δ^{36}S, ‰	Location
Bogou	IAB-MG	0.252	0.010	−0.006	UMD
Bogou*	—	−0.408	0.012	−0.043	IPGP
Campo del Cielo	IAB-MG	−0.168	0.004	0.129	UMD
Campo del Cielo (AVS2)	—	−0.137	0.008	0.253	UMD
Campo del Cielo*	—	−0.185	−0.004	0.084	IPGP
Canyon Diablo	IAB-MG	−0.277	0.003	0.209	UMD
Canyon Diablo	—	0.118	0.011	0.039	IPGP
Mudrabilla-2	IAB-Mund	0.128	−0.003	−0.036	UMD
Mundrabilla	—	−0.127	−0.007	0.110	UMD
Mundrabilla*	—	−0.072	−0.005	0.018	IPGP
Waterville	IAB-Mund	−0.228	0.002	0.068	UMD
Waterville*	—	−0.198	0.005	−0.051	IPGP
Pitts	IAB-Pitts	−0.319	−0.002	0.207	UMD
Pitts*	—	0.005	0.003	0.045	IPGP
Goose Lake	IAB-sLL	−0.167	0.003	0.181	UMD
Goose Lake (AVS2)	—	−0.247	0.006	0.282	UMD
Goose Lake*	—	0.042	0.000	0.068	IPGP
Mertzon	IAB-ung	−0.171	0.010	0.124	UMD
Mertzon (AVS2)	—	−0.277	0.009	0.277	UMD
Mertzon*	—	−0.097	−0.001	0.042	IPGP
Mesa Verde Park	IAB-Ung	0.139	0.007	0.226	UMD
Mesa Verde Park*	—	−0.668	0.005	−0.019	IPGP
Santa Rosa	IC	0.008	0.017	−0.070	UMD
Santa Rosa-2	—	−0.087	0.017	−0.064	UMD
Santa Rosa	—	0.229	−0.002	−0.150	IPGP
Watson	IIE	−0.361	0.009	0.106	UMD
Watson	—	0.007	0.011	−0.068	IPGP
Costilla Peak	IIIAB	−0.562	0.018	−0.053	UMD
Costilla Peak	—	0.113	0.017	−0.120	IPGP
Cerro del Inca	IIIF	−0.117	−0.027	−0.233	UMD
Cerro del Inca	—	0.463	−0.033	−0.100	IPGP
Hoba	IVB	−0.485	0.000	0.128	UMD
Hoba	—	−0.648	−0.015	−0.136	IPGP
Average Difference (from Abs. Values)		**0.339**	**0.006**	**0.136**	

*Denotes AVS + CRS extraction at IPGP; all other samples represent AVS data. For these measurements, UMD data represent counting statistics 9 times greater than IPGP. Average differences are in bold.

Table S5. Two-tailed heteroscedastic T-tests

	P value			n value	
Pairing	δ^{34}S	Δ^{33}S	Δ^{36}S	Group 1	Group 2
IIIAB-IAB	3.89E-01	**1.05E-10**	**4.56E-05**	$n = 18$	$n = 27$
IVA-IAB	**1.95E-02**	**1.14E-06**	**2.04E-02**	$n = 9$	$n = 27$
IIAB-IAB	8.27E-01	**1.55E-05**	**8.96E-04**	$n = 10$	$n = 27$
IVA-IIAB	**1.96E-02**	**3.81E-02**	1.29E-01	$n = 9$	$n = 10$
IVA-IIIAB	**8.63E-03**	9.34E-02	3.16E-01	$n = 9$	$n = 18$
IIAB-IIIAB	6.19E-01	4.34E-01	3.96E-01	$n = 10$	$n = 18$
Magmatic-Non-Magmatic	6.15E-01	**1.64E-04**	**2.73E-07**	$n = 44$	$n = 29$

*P values lower than 0.05 are in bold.

Table S6. Ly-α vertical optical depths for high-mass and low-mass disks with 1-μm dust

Disk type	Time, y	Z, AU	$n_H(Z)$, cm^{-3}	N_H, cm^{-2}	τ_{H2O} (solar)	τ_{H2O} (C/O = 1.5)	τ_{H2S}	τ_{dust}
High-mass	$<5 \times 10^4$	0.15	5.5×10^{13}	1.3×10^{25}	2.5×10^4	8.3×10^3	4.7×10^3	4.4×10^3
		0.2	6.5×10^{12}	1.3×10^{24}	2.5×10^3	830	470	440
		0.25	4.2×10^{11}	7.6×10^{22}	150	50	28	25
		0.3	1.5×10^{10}	2.3×10^{21}	4.4	1.5	0.84	0.77
		0.35	2.8×10^8	4.0×10^{19}	0.077	0.026	0.015	0.013
Low-mass	$<5 \times 10^5$	0.1	2.2×10^{13}	4.2×10^{24}	8.1×10^3	2.7×10^3	1.5×10^3	1.4×10^3
		0.15	2.2×10^{12}	3.9×10^{23}	750	250	140	130
		0.2	8.6×10^{10}	1.3×10^{22}	25	8.3	4.7	4.4
		0.25	1.3×10^9	1.6×10^{20}	0.31	0.1	0.058	0.054
		0.3	8.3×10^6	9.3×10^{17}	0.0018	0.0006	3.4×10^{-4}	3.1×10^{-4}